Historical surface mass balance reconstruction 1984 – 2017 from GreenTrACS multi-offset ground-penetrating radar

Tate G. MEEHAN,[1,2] H.P. MARSHALL,[1,2] John H. BRADFORD,[3] Robert L. HAWLEY,[4] Thomas B. OVERLY,[5,6] Gabriel LEWIS,[4] Karina GRAETER,[4] Erich OSTERBERG,[4] Forrest McCARTHY [4]

[1]*Department of Geoscience, Boise State University, Boise, ID, USA*

[2] *U.S. Army Cold Regions Research and Engineering and Laboratory, Hanover, NH, USA*

[3]*Department of Geophysics, Colorado School of Mines, Golden, CO, USA*

[4]*Department of Earth Sciences, Dartmouth College, Hanover, NH, USA*

[5]*Cryospheric Sciences Lab, NASA Goddard Space Flight Center, Greenbelt, MD, USA*

[6]*Earth System Science Interdisciplinary Center, University of Maryland, College Park, MD, USA*

Correspondence: Tate Meehan <tatemeehan@u.boisestate.edu>

S.1. SUPPLEMENTARY MATERIAL

We introduced the methodological concepts of our radar measured and modeled approach for reconstructing historical SMB in Section 3. Within supplement S.1, we provide the core computations used and give more insight into the methods of velocity analysis, parameter estimation, imaging, and interpretation. The flow diagram (Fig. S.1) works through the MxHL process to show not only the radar processing steps, but also the interconnectivity between the radar measured information and the HL firn model.

We introduce our methods for interpreting the radar imagery (Section S.1.1) and conducting horizon velocity analysis (Section S.1.2). We use the radar wave velocity information for snow parameter estimation (see sections S.1.3 and S.1.4), and use these results to parameterize the MxHL model in Section S.1.5. We then extend the capabilities of the firn age and density models to enable our structure-oriented filter (see section S.1.6) and refine our estimate of SMB using relative age model updates in the stratigraphic age domain (Wheeler, 1958) and absolute age model updates in the depth domain (see section S.1.7).

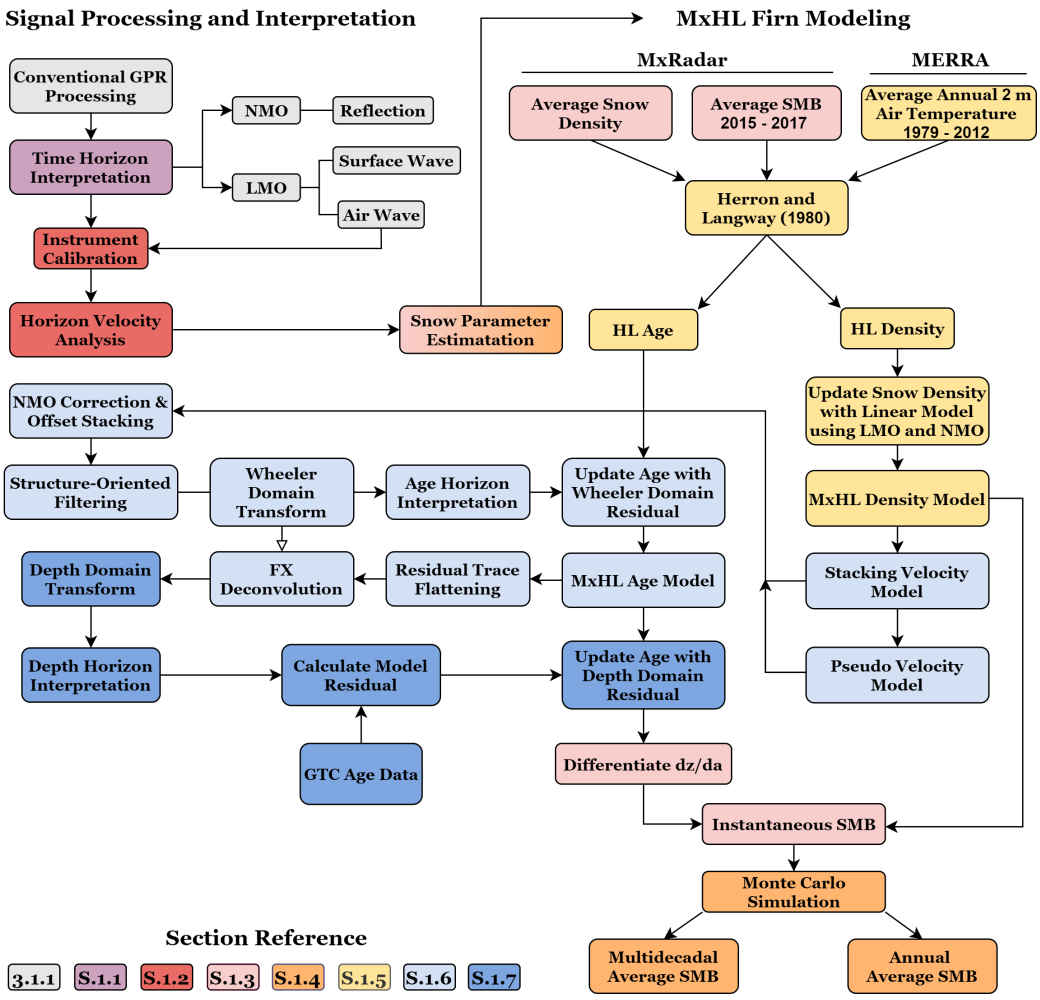

Fig. S.1: The workflow for our measured-modeled historical SMB reconstruction. Colors correspond to the section reference where the concept is detailed. For example, the gradient colors of *Snow Parameter Estimation* indicate that concept spans sections S.1.3 and S.1.4.

S.1.1. Travel-time Horizon Interpretation

We developed a phase and amplitude tracking, semi-automatic picking algorithm to measure the travel-times of radar wavefield events. The picker is semi-automatic in that an initial pick on the horizon seeds the automatic tracking. Similar to picking algorithms described by Dorn (1998), our seeded picker transforms a window of the radargram surrounding the horizon of interest into radial distance and dip angle coordinates (r, θ) and stacks the windowed image along the θ direction. The algorithm determines the optimal direction by maximizing stacked amplitude. The subsequent automatic pick is predicted 5 traces ahead, which is approximately the length of the radar array, along the linear path of maximum stack. Then the windowed polar transformation and prediction is repeated automatically. Travel-time picks between predictions are interpolated using a distance-weighted scheme. The program has the capability to toggle manual selection or re-seed the pick if the algorithm goes awry. We picked the direct air wave, the direct surface wave, and

the reflected wave from the fall 2014 layer on each of the nine radargrams for velocity analysis. These early-time events exhibit low noise with a travel-time standard deviation of 0.2 ns (1 sample). Using this layer picker, we also picked five age-horizons (see section S.1.6) and 16 depth-horizons (see section S.1.7) to update the age model for SMB calculation.

S.1.2. Horizon Velocity Analysis

Direct (air-coupled and surface-coupled) waves obey the linear travel-time equation known as linear moveout (LMO)

$$t = t_0 + \frac{x}{V_{LMO}} \quad , \tag{S.1}$$

where t is the measured one-way travel time and x is the antenna offset, with intercept time (t_0) and velocity (V_{LMO}) representing unknown parameters. Reflected radar waves exhibit non-linear travel-times as a function of offset that are approximated by NMO. The $x^2 - t^2$ method (Green, 1938) linearizes the NMO equation

$$t^2 = t_0^2 + \frac{x^2}{V_{NMO}^2} \quad . \tag{S.2}$$

where t is now the measured two-way travel time and V_{NMO} is the NMO velocity or *stacking velocity*.

Prior to velocity analysis of the surface wave and reflection, we calibrated the timing of each radar channel. Channel consistent travel-time overheads are caused within the Sensors & Software multi-channel adapter by variations in the path lengths of the circuitry and cables. During the instrument calibration process we apply corrections (on the order of nanoseconds) to the time sampling of each channel by picking the air-wave arrival times (Fig. 4) and solving Eq. (S.1) for the set of perturbations that let $t_0 = 0$ and $V_{LMO} = 0.2998\ m/ns$, the velocity of EM waves in free-space.

We applied linear regression for near-surface velocity analyses using the picked, one-way travel-times of direct wave arrivals traveling laterally through the shallow snow and the two-way travel-times of reflected arrivals from the fall 2014 horizon. To cast each system of equations into a matrix-vector product, the velocity parameter is linearized by its reciprocal, called slowness, as $S = \frac{1}{V}$. The linear system of equations has the form $\mathrm{G}\mathbf{m} = \mathbf{d}$ for the vector $\mathbf{d}$ containing the recorded travel-times for the respective moveout events. Equations (S.3) and (S.4) are the monomial basis functions used for linear regression of LMO and NMO events. Equations (S.5) and (S.6) are the model parameters and equations (S.7) and (S.8) are the

respective data. The least squares solution for $\mathbf{m} = \mathrm{G}^{-1}\mathbf{d}$ is optionally solved in either L_2 or L_1 norm. We used the L_2 solution which was estimated by QR factorization (Businger and Golub, 1965). Advantages and convergence criteria of the L_1 solution are discussed in Aster and others (2019).

$$\mathrm{G_{LMO}} = \begin{bmatrix} 1 & x_1 \\ \vdots & \vdots \\ 1 & x_m \end{bmatrix} \quad \text{(S.3)} \qquad \mathbf{m}_{\mathrm{LMO}} = \begin{bmatrix} t_0 \\ \\ S_{LMO} \end{bmatrix} \quad \text{(S.5)} \qquad \mathbf{d}_{\mathrm{LMO}} = \begin{bmatrix} t_1 \\ \vdots \\ t_m \end{bmatrix} \quad \text{(S.7)}$$

$$\mathrm{G_{NMO}} = \begin{bmatrix} 1 & x_1^2 \\ \vdots & \vdots \\ 1 & x_m^2 \end{bmatrix} \quad \text{(S.4)} \qquad \mathbf{m}_{\mathrm{NMO}} = \begin{bmatrix} t_0^2 \\ \\ S_{NMO}^2 \end{bmatrix} \quad \text{(S.6)} \qquad \mathbf{d}_{\mathrm{NMO}} = \begin{bmatrix} t_1^2 \\ \vdots \\ t_m^2 \end{bmatrix} \quad \text{(S.8)}$$

S.1.2.1. Critically Refracted Waves

A snowpack model with a critically refracted raypath is sketched in Fig. S.2. The following exercise calculates the travel-time of the wave following the hypothesized path.

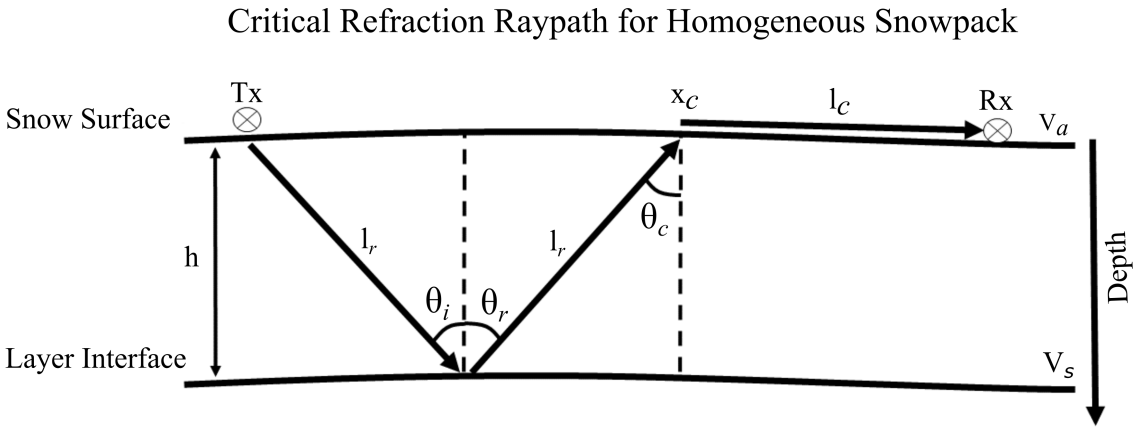

Fig. S.2: The raypath of a critically refracted wave traveling through a homogeneous snowpack. The wave is reflected at a layer boundary in the firn and is refracted upon exiting the snow surface.

The snowpack is homogeneous with a thickness (h) and EM velocity (V_s). A half-space of air (V_a) is modeled above the snow surface. The transmitter and receiver antennas are on the snow surface and are separated by some offset (x). In a homogeneous medium at a reflecting interface, the reflection angle (θ_r) is equal to the incidence angle (θ_i). Except for the case of total reflection, incoming radiation is also refracted

(transmitted) at the layer interface. When a wave is traveling from a slower medium to a faster medium, according to Snell's Law

$$\frac{\sin\theta_1}{\sin\theta_2} = \frac{V_1}{V_2} \quad , \tag{S.9}$$

there is an angle of incidence that causes a critical refraction, known as the critical angle (θ_c). Critically refracted energy is refracted at 90° and travels along the interface boundary within the faster medium. By setting $\theta_2 = 90°$,

$$\frac{\sin\theta_c}{\sin 90} = \frac{V_1}{V_2} \quad , \tag{S.10}$$

$$\theta_c = \sin^{-1}\left(\frac{V_1}{V_2}\right) \quad , \tag{S.11}$$

68 θ_c is solved.

In Fig. S.2, $\theta_i = \theta_r = \theta_c$. A critical refraction occurs along the free-surface boundary when this equality is satisfied. The critical distance (x_c) can be solved,

$$x_c = h \cdot \tan\theta_c \quad , \tag{S.12}$$

when θ_c and h are known. The refraction path length

$$l_c = x - x_c \quad , \tag{S.13}$$

69 and the NMO reflection path length $2l_r$, where

$$l_r = \sqrt{\left(\frac{x_c}{2}\right)^2 + h^2} \quad , \tag{S.14}$$

are summed to calculate the refracted raypath length

$$l = 2l_r + l_c \quad . \tag{S.15}$$

The travel-time

$$t_c = \frac{2l_r}{V_s} + \frac{l_c}{V_a} \quad , \tag{S.16}$$

70 from Tx to Rx is calculated for any offset beyond x_c.

71 Travel-times calculated from this model can be used to identify the refracted waves in Fig. 4. Residual
72 travel-time corrections are not applied to Fig. 4. Add these approximate travel-time corrections to the

data gather when comparing the modeled travel-times: $(4\ m) \sim 1\ ns$, $(8\ m) \sim 1.5\ ns$, $(12\ m) \sim 3\ ns$. For reference, 0.5 wavelet cycles is ~ 0.5 ns.

S.1.3. Parameter Estimation: Depth, Density, and SMB

The wave propagating along the ice sheet surface is estimated to respond to snow depths no greater than the wavelength

$$z_{LMO} = \frac{V_{LMO}}{f} \quad , \tag{S.17}$$

calculated from the nominal radar frequency ($f \approx 500\ MHz$) and snow velocity (V_{LMO}). Eq. (S.17) was developed on Occam's razor. This simple approximation for the penetration of the surface coupled wave was found to be consistent with the depth and average density measured at GTC15 and Pit 15 W. The depth of the reflection horizon for a subsurface propagating wave

$$z_{NMO} = \frac{V_{NMO} \cdot t_0}{2} \quad , \tag{S.18}$$

is estimated assuming that the NMO approximation is valid, meaning that V_{NMO} is approximately equal to the average velocity above the horizon.

The complex refractive index method (CRIM) equation relates a mixture of known dielectric properties to an estimated effective bulk property (Wharton and others, 1980). We estimated the average snow density from the EM velocity by the CRIM equation

$$\rho_s = \rho_i \left(1 - \frac{V_a(V_i - V_s)}{V_s(V_i - V_a)}\right) \quad , \tag{S.19}$$

letting the snow and firn pore space be unoccupied free space with the velocity $V_a = 0.2998\ m/ns$ and the matrix to be composed of only ice with EM velocity $V_i = 0.1689\ m/ns$, and density $\rho_i = 917\ kg/m^3$ (Ulaby and others, 1986). The quantities are given the subscript a for air, i for ice, or s for snow and firn. Liquid water within the firn layer was neither present within snow pits nor firn cores sampled during this field study, and is therefore not considered in Eq. (S.19).

Surface mass balance is conventionally measured using GPR by interpreting a select few IRHs using a constant age interval and applying the average normalized snow and firn density over this interval (e.g. Lewis and others, 2019). Instead, we rely on the models of density and age, which are discretized in depth

at a comparable resolution to the GPR data. We measured instantaneous SMB ($\dot{b}$), in meters of water equivalent per an infinitesimal time

$$\dot{b} = \frac{\rho_s}{\rho_w} \frac{\mathrm{d}z}{\mathrm{d}a} \quad , \tag{S.20}$$

as the product of the snow and firn density, normalized by the density of water (ρ_w), and the submergence rate of stratigraphic isochrones $\left(\frac{\mathrm{d}z}{\mathrm{d}a}\right)$ in a Lagrangian reference frame. The submergence rate is the continuous equivalent of interpreting a few horizons with large age intervals. In practice, we approximated this derivative using second-order accurate finite difference weights calculated from the Fornberg (1988) algorithm, because the age-depth model is not discretized in regular intervals. The median discrete interval of the age-depth model is 14 days with a minimum interval of seven days and a maximum interval of 20 days. We found that the local truncation error of the second-order accurate derivative was 5×10^{-5} m $w.e.$ a^{-1}, which has a leading error term an order of magnitude less than what we consider to be significant.

S.1.4. Parameter Uncertainty: Monte Carlo Bootstrapping and Error Propagation

To ascertain the uncertainty in the radar inversion, we implemented a bootstrapping algorithm by randomly sub-sampling the CMP travel-times from the LMO and NMO horizons and re-solving the linear regression. In a roll-along fashion, travel-time observations of five neighboring CMP gathers were binned and re-sampled by removing two offsets at random and then randomly sampling one travel-time observation for each remaining offset in the bin. This algorithm creates many realizations of the intercept time and snow velocity by the jackknife technique (Efron and Stein, 1981). Realizations of depth and density were generated from the current realization of $\mathbf{m}$ following Equations (S.17) – (S.19). The bootstrapped distribution $\widehat{\mathcal{M}}$ was generated from 1000 jackknifed realizations to establish uncertainty regions (Efron and Tibshirani, 1986). A distribution was gathered for each parameter: intercept travel-time, velocity, depth, and density. The mean of $\widehat{\mathcal{M}}$ yields the expected value of the parameter ($\widehat{m}$) with a standard deviation ($\widehat{\sigma}$). We developed uncertainty regions for each bootstrapped distribution assuming the standard normal distribution

$$\widehat{m} \pm \widehat{z}\,\widehat{\sigma} \quad , \tag{S.21}$$

and assessed the z-score at $\widehat{z} = 1$, which has the central interval of $1\widehat{\sigma}$ (Efron and Tibshirani, 1986). The jackknifed estimates of variance for snow density and depth provide the means to estimate uncertainty in the $2015 - 2017$ SMB. We estimated the variance of SMB by the linear error propagation equation

$$\widehat{\sigma}_{\dot{b}}^2 = \widehat{\sigma}_z^2 \rho^2 + \widehat{\sigma}_\rho^2 z^2 + 2\widehat{\sigma}_{\rho z} \rho z \quad , \tag{S.22}$$

where the covariance $\widehat{\sigma}_{\rho z}$ was calculated from the parameter distributions. The resulting uncertainty measure is the standard interval developed from Eq. (S.21). The snow parameters and uncertainties presented in Fig. 5 were smoothed using a Gaussian kernal with a standard deviation of 250 m.

As we presented in Fig. 9, we propagated uncertainties in SMB by Monte Carlo simulation, which incorporated the uncertainty in the age of dated isochrones ($\sigma_a = \pm 31$ days) and the uncertainties in the snow parameters used to generate the firn model (Section S.1.5). We estimated the ± 31 day uncertainty by summing in quadrature the uncertainties in the firn core age (± 18 days; Rupper and others (2015)) and the radar estimated depth that was mapped to the GTC15 age-depth scale (± 25 days) developed by Lewis and others (2019). We delimited the annual SMB calculation between January 1, 1984 and January 1, 2017, which are the complete years between the date of the earliest layer picked and the date of data acquisition. We filtered the outlying 1% of the instantaneous SMB model and interpolated between neighboring values. We quantified annual average SMB and its uncertainty using Monte Carlo simulation, by generating 1000 randomly initialized density-depth models (Section S.1.5) from the snow parameter distributions. Rather than randomly generating an age model in this process, because we updated the age-depth model by interpreting IRHs (Section S.1.6), we interpolated the age model to the depth axis that was defined by the Monte Carlo realization of the density model. We calculated the numerical derivative to estimate the instantaneous SMB (Eq. (S.20)), extracted the intervals that composed each annual layer, and averaged the samples of instantaneous SMB into one realization of annual SMB. After 1000 realizations were generated for each of 33 years in the period $1984 - 2017$, we calculated the multidecadal mean SMB and variance using Monte Carlo resampling. Repeating for 1000 simulations, we randomly sampled an annual SMB realization from 10 annual intervals and averaged. In the following section, to clarify the capabilities of the radar analysis we ignore the uncertainties in the firn core ages and demonstrate the radar inversion as the only source of uncertainty in SMB when paramertizing the MxHL model.

S.1.5. Parameterizing the MxRadar - Herron and Langway (1980) Model

The Herron and Langway (1980, HL) model requires three parameters: mean snow density, mean annual accumulation, and 10 m firn temperature. We use the snow properties estimated by the radar inversion (Fig. 5) and MERRA reanalysis temperature to parameterize the HL model in our measured-modeled, MxRadar-HL, framework. We chose the density parameter as the average of the densities estimated by the surface-wave (LMO) analysis and the reflected wave (NMO) analysis of the fall 2014 isochronous reflection horizon (IRH). We approximated the accumulation parameter using the radar estimated SMB (Eq. (S.20)) that represented the average of the previous ~ 2.5 years – as the IRH depth indicates the date November 30, 2014, established by the firn core analysis, and the date of acquisition was June 13, 2017. Mean annual 2 m air temperature was calculated from MERRA $(1979-2012)$ data (Birkel, 2018) and used as a proxy for 10 m firn temperature (Loewe, 1970). MERRA annual temperatures at GTC15 over the period $1979-2012$ show an increase of $0.06 \pm 0.01\ ^{\circ}C\ a^{-1}$ with a mean of $-25.7 \pm 1.0\ ^{\circ}C$.

We evaluated the MxHL parameterization by comparing it to the GTC15 parametization (Fig. S.3) and an optimum set of parameters that were determined by minimizing

$$\phi = \frac{\mathrm{RMS}(\tau_{HL} - \tau_{GTC15})}{\mathrm{range}(\tau_{GTC15})} + \frac{\mathrm{RMS}(\rho_{HL} - \rho_{GTC15})}{\mathrm{range}(\rho_{GTC15})} \quad , \tag{S.23}$$

using the Nelder and Mead (1965) method (NM) for nonlinear optimization. The objective function ϕ (Eq. (S.23)) measures the root-mean-squared error of the modeled (HL) and measured (GTC15) age (τ) and density (ρ) as a percentage, normalized by the range in the data for the entire depth of GTC15 ($\sim 28.5\ m$). An objective function measured by either τ or ρ individually does not contain a unique global solution upon minimization. We found that an appropriate fit to GTC15 τ or GTC15 ρ could be achieved with a range of parameterizations, alluding to the non-uniqueness which we regularized by minimizing ϕ as a function of both the age and density.

Average SMB, density, and 10 m bore hole temperature measured at GTC15 provided the true parameterization for the HL model. The age-depth scale (1969-2017) was measured by analyzing seasonal oscillations of δ^{18}O, major ions, and dust observed in the firn core (Lewis and others, 2019). Annual SMB was measured by combining the age-depth scale with the firn density (Lewis and others, 2019). We estimated the GTC15 mean annual SMB using Monte Carlo resampling to assess uncertainties ($0.306 \pm 0.021\ m\ w.e.\ a^{-1}$). We chose the GTC15 density parameter ($359 \pm 36\ kg/m^3$), which is the "commonly reported average density over the first one or two meters of snow" (Herron and Langway, 1980,

p. 7), at the interval that had the minimum residual with the NM optimum density. The central depth of the core interval nearest to the optimal density is 1.22 ± 0.13 m. Uncertainties in the density parameter are assumed to be within 10% of the measurement. We measured firn temperatures using borehole thermistors at 6, 8, 10, 12, and 14 m depth. After the thermistor string reached equilibrium, temperatures between 6 and 14 m depth closely agreed and we used Monte Carlo resampling to estimate the 10 m firn temperature (-24.9 ± 0.2 $°C$).

The HL model parameterized by GTC15 data yielded $\phi = 6.4\%$, which is near the optimum $\phi = 6.2\%$. The MxHL parameters obtained in the vicinity of GTC15 achieved an agreeably close fit with $\phi = 7.0\%$. Table S.1 summarizes the three HL model parameterizations and their accuracy. Figure S.3 displays the MxHL parameters overlaid on slices of Eq. (S.23) through the GTC15 parameters.

We completed the radar analyses using the MxHL model after making the following adjustments. We refined the density model using the LMO and NMO derived densities and depths to estimate the snow density-depth gradient. Using a linear model we replaced the upper one to two meters of the HL model with a piecewise segment that was extrapolated to the surface and merged with the HL model at the intersecting depth in the snow. We also refined the age model and improved the radar image quality using structure-oriented filtering (see section S.1.6).

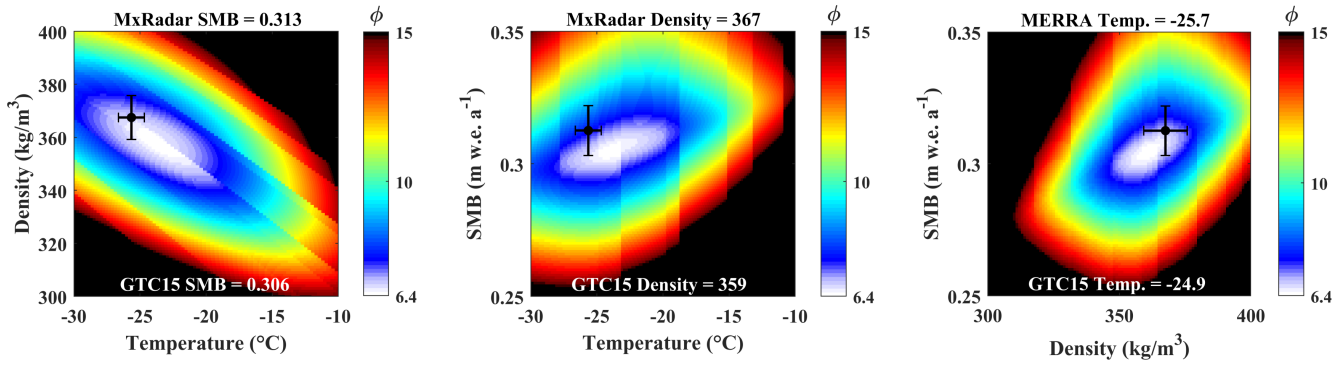

Fig. S.3: Equation S.23 is represented as slices through the GTC15 parameterization. Viewing the 3D objective function this way shows the model sensitivity to the parameters. The MxHL parameters are evaluated against the GTC15 parameterization with 1σ uncertainties. These data are summarized in Table S.1.

Table S.1: HL parameters from MxRadar (MxHL), GreenTrACS Core 15 (GTC15), and Nelder and Mead (1965) optimization (NM) are compared. Uncertainties in the GTC15 and MxHL parameterizations are expressed at 1σ. Accuracy is reported for the modeled age (ϕ_τ) and density (ϕ_ρ) as the rms error and jointly as the normalized summed rms error ϕ.

Parameters	$\dot{\mathbf{b}}$ **(m w.e. a^{-1})**	ρ **(kg/m^3)**	**T ($^\circ$C)**	τ_{RMSE} **(a)**	ρ_{RMSE} **(kg/m^3)**	ϕ (%)
MxHL	0.313 ± 0.009	367 ± 8	-25.7 ± 1.0	0.528	20.2	7.0
GTC15	0.306 ± 0.021	359 ± 36	-24.9 ± 0.2	0.40	20.0	6.4
NM	0.306	358	-23.1	0.350	19.0	6.2

S.1.6. Structure-oriented Filtering in the Wheeler Domain

Accumulated snow is deposited in isochronous layers that propagate slowly as the firn stratigraphy evolves and are apparent in the radiostratigraphy (Arcone and others, 2005; Ng and King, 2011). However, as demonstrated in this study, larger amplitude stratigraphic undulations with wavelengths of $\lessapprox 5\ km$ exhibit reduced coherence in the GPR imaging, an effect that is worsened by increased surface roughness. As described by Arcone and others (2004), artificial fading in the GPR image along the limbs of stratigraphic folds also interrupts the horizon continuity. The fading effect can be seen in Fig. 8 as a discontinuity in the inflection point of a fold at 48 km distance and $\sim 11\ m$ depth. It is important to accurately capture SMB variability at $< 5\ km$ for evaluating downscaled surface mass balance models, but as we demonstrate, this effort would be limited to only a few horizon selections here because of noise contamination in the radar section.

Structure-oriented filtering techniques often determine the structure from the time or depth image by localized eigenvalue decomposition of the image gradient tensor, such as filters applying nonlinear anisotropic diffusion (Fehmers and Höcker, 2003). We imposed the isochrone structure on the image, using the age model as a proxy for the stratigraphic structure. We flattened the firn structure by converting the time domain GPR image into coordinates of stratigraphic age, known as the Wheeler (1958) domain. We then applied linear prediction filtering, because flattening the traces improves their predictability by linear modeling. Conversion to stratigraphic coordinates can be achieved using plane wave deconstruction filters to determine local slope fields from the image (Karimi and Fomel, 2015). But it is to our advantage to work with the stratigraphic age because this information is necessary for SMB calculations. We found our approach outperformed filters that determine the structure orientation directly from the noisy image.

To implement the structure-oriented filter, we produced a noisy time domain radar section from the multi-channel imagery (Fig. 7) by first transferring the measured-modeled firn density to stacking velocity (V_{NMO}) and then applying normal moveout correction and offset stacking (Yilmaz, 2001). Provided that the radiostratigraphy in depth mimics the firn layering and is isochronous (e.g. Spikes and others, 2004), we used the HL age-depth model to estimate the firn structure orientation and age. To do so, we first converted the age model from depth to travel-time (Fig. S.4) by a vertical stretch (Margrave and Lamoureux, 2019) using the stacking velocity model. We created a pseudo stacking velocity model (V_{pseudo}) with units of years per nanosecond by dividing the age-travel-time model by the two-way travel times. Then we converted the radar image from travel-time to the Wheeler domain by a vertical stretch using V_{pseudo} (Fig. S.5). We oversampled

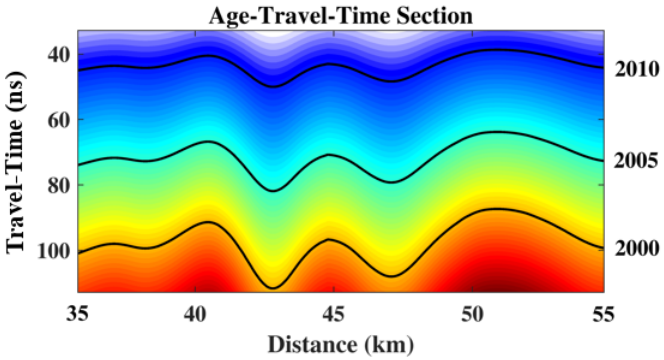

Fig. S.4: The age-travel-time model was calculated from pseudo velocities. Contours of this image are isochronous travel-time horizons. January 1, 2010, 2005, and 2000 are labeled for reference. We used the age-travel-time model to flatten the radar traces, by converting the time domain image into the age domain (Fig. S.5).

in the Wheeler domain to prevent signal aliasing. The age converted radargram has approximately flattened stratigraphy, such that any row of the image is isochronous. If we knew the structure orientation perfectly, and radar isochrones truly had the same age, the layers in the Wheeler domain would be theoretically flat. By picking, we calculated the residual age of five IRHs with an average epoch of 5.3 ± 2.7 years (the latest being the 1991 horizon) and used 1D shape preserving piecewise interpolation polynomials (Kahaner and others, 1989) to create a grid of perturbations for the age-travel-time model (Fig. S.6). Perturbations beyond the last picked horizon were set to zero. We applied the perturbations to the age model and re-flattened the image by stretching the traces to the updated age model (Fig. S.7). Radar amplitudes are now approximately horizontal across each row of the Wheeler domain image, indicating that the age-travel-time model fits the firn structure and IRH theory.

We applied the fx-deconvolution noise suppression algorithm (Gulunay, 1986) to the Wheeler domain radargram (Fig. S.8). Fx-deconvolution relies on autoregression modeling of the GPR signal in the frequency domain to build the optimal complex Wiener filter (Treitel, 1974). We applied the filter by averaging overlapping computations along the age axis to alleviate non-stationarity of the signal frequency. This process can benefit any GPR imagery of polar firn, provided that an initial stratigraphic age model, as a proxy for the structure, and methods to convert the image domain are available. At GTC15 Spur West, due to the large spatial gradient in SMB, it was necessary to determine the model residual and re-flatten the image before filtering. For GPR imagery expressing small or gradual SMB variability it may be sufficient to apply the structure-oriented filter without residual corrections to the Wheeler image.

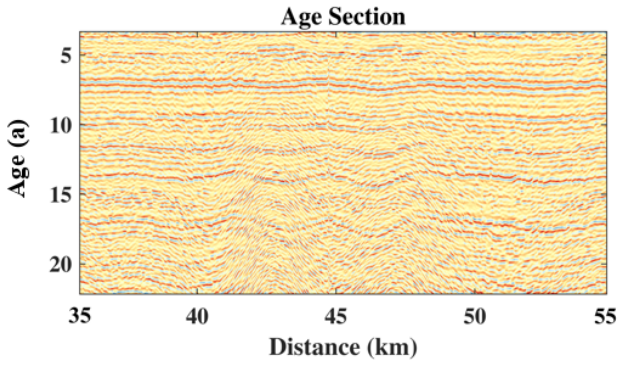

Fig. S.5: Using the initial age model, the Wheeler domain radargram has minor remnant undulations. Because the rows of the Wheeler image are isochronous, the undulations that deviate from row-wise horizontal are the model residual. If the age model was correct the radar reflections would be entirely horizontal (Fig. S.7). By interpreting five horizons of this image, we interpolated the model residual (Fig. S.6) and applied these perturbations to update the age model such that it is accurate in a relative sense.

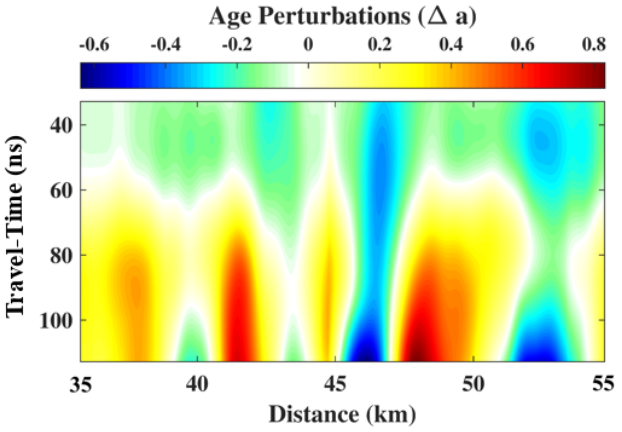

Fig. S.6: Perturbations in the travel-time domain are calculated by picking IRHs in Fig. S.5. When applied, the Wheeler domain image is reflattened (Fig. S.7), which ensures that the age model is accurate in a relative sense. We rely on ages measured from the firn core for absolute accuracy in the age model.

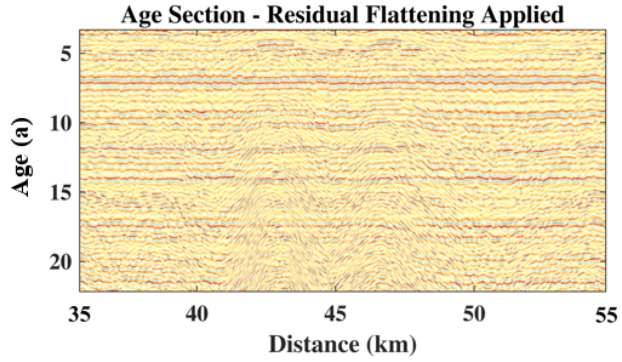

Fig. S.7: After interpreting five horizons of Fig. S.5, calculating the model residual (Fig. S.6), and applying the perturbations to the age-travel-time model (Fig. S.4), we re-flattened the Wheeler image. The radar amplitudes are now approximately horizontal, indicating that the updated age model is accurate according to the IRH theory.

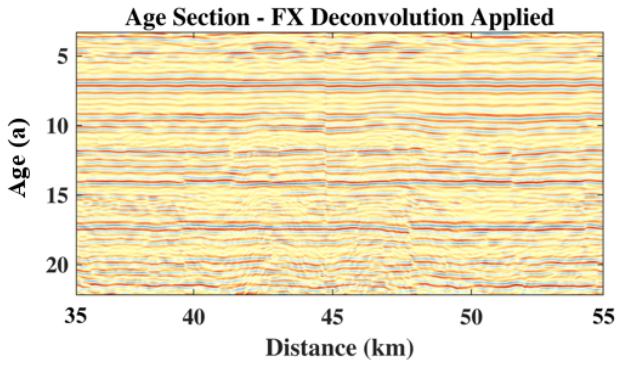

Fig. S.8: Flattening the traces improves their predictability by linear modeling. We applied the fx-deconvolution algorithm (Gulunay, 1986) to suppress the random noise that contaminates the linearly predictable signal.

S.1.7. Depth Imaging for Model Updates

We converted the updated age-travel-time model to depth using the stacking velocity model and then we used the age-depth model to convert the Wheeler domain image to depth. We applied a vertical stretch for each conversion operation (Margrave and Lamoureux, 2019). Figure 8 reveals the smooth and continuous IRHs of the depth image. The additional step of structure-oriented filtering extended the interpretable isochrone record from 1991 to 1984 (which is only limited by the time-window range of the radar acquisition). We picked 16 IRHs on the depth image with an average epoch of 2.1 ± 1.7 years. Over an equivalent depth range, this compares to the seven IRHs at five year age resolution used by Lewis and others (2019) to estimate SMB along GTC15 Spur West. In the vicinity of GTC15 the residuals between the GTC15 age-depth scale and the picked IRH ages were calculated. We created a second set of age perturbations using 1D linear interpolation with linear extrapolation to estimate perturbations beyond the deepest picked IRH (Fig. S.9), and we applied these perturbations to update the age-depth model. We then used the updated age model to calculate the instantaneous SMB.

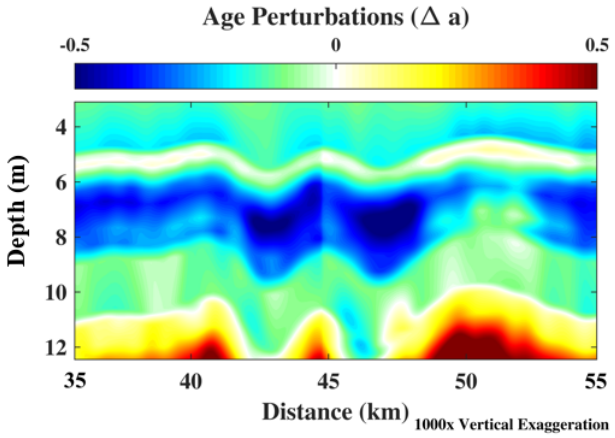

Fig. S.9: We interpreted 16 IRHs of Fig. 8 to measure their relative age at depth. We calculated the residual between our interpreted ages and the ages measured from GTC15 and interpolated this grid of perturbations in the depth domain. We applied these perturbations to the age-depth model which was used to calculate the SMB time-series. Applying this set of perturbations makes the relative age-depth model accurate in an absolute sense.

REFERENCES

Arcone SA, Spikes VB, Hamilton GS and Mayewski PA (2004) Stratigraphic continuity in 400 MHz short-pulse radar profiles of firn in West Antarctica. *Ann. Glaciol.*, **39**(2002), 195–200, ISSN 02603055 (doi: 10.3189/172756404781813925)

Arcone SA, Spikes VB and Hamilton GS (2005) Stratigraphic variation within polar firn caused by differential accumulation and ice flow: Interpretation of a 400 MHz short-pulse radar profile from West Antarctica. *J. Glaciol.*, **51**(174), 407–422, ISSN 00221430 (doi: 10.3189/172756505781829151)

Aster RC, Borchers B and Thurber CH (2019) *Parameter estimation and inverse problems*. Elsevier

Birkel S (2018) Greenland surface mass balance derived from climate reanalysis models, 1979-2017 (doi: 10.18739/A2D21RH75)

Businger P and Golub GH (1965) Linear least squares solutions by householder transformations. *Numer. Math.*, **7**(3), 269–276, ISSN 0029-599X (doi: 10.1007/BF01436084)

Dorn GA (1998) Modern 3-D seismic interpretation. *Lead. Edge*, **17**(9), 1262–1262, ISSN 1070-485X (doi: 10.1190/1.1438121)

Efron B and Stein C (1981) The Jackknife Estimate of Variance. *Ann. Stat.*, **9**(3), 586–596, ISSN 0090-5364 (doi: 10.1214/aos/1176345462)

Efron B and Tibshirani R (1986) Bootstrap Methods for Standard Errors, Confidence Intervals, and Other Measures of Statistical Accuracy. *Stat. Sci.*, **1**(1), 54–77, ISSN 0883-4237, 2168-8745 (doi: 10.1214/ss/1177013815)

Fehmers GC and Höcker CF (2003) Fast structural interpretation with structure-oriented filtering. *Geophysics*, **68**(4), 1286–1293, ISSN 00168033 (doi: 10.1190/1.1598121)

Fornberg B (1988) Generation of Finite Difference Formulas on Arbitrarily Spaced Grids. *Math. Comput.*, **51**(184), 699, ISSN 00255718 (doi: 10.2307/2008770)

Green CH (1938) Velocity Determinations by Means of Reflection Profiles. *Geophysics*, **3**(4), 295–305, ISSN 0016-8033 (doi: 10.1190/1.1439508)

Gulunay N (1986) FXDECON and complex wiener prediction filter. In *SEG Tech. Progr. Expand. Abstr. 1986*, 279–281, Society of Exploration Geophysicists (doi: 10.1190/1.1893128)

Herron MM and Langway CC (1980) Firn Densification: An Emperical Model. *J. Glaciol.*, **25**(93), 373–385, ISSN 00221430

Kahaner D, Moler C and Nash S (1989) Numerical methods and software. *Englewood Cliffs Prentice Hall, 1989*

Karimi P and Fomel S (2015) Stratigraphic coordinates: A coordinate system tailored to seismic interpretation. *Geophys. Prospect.*, **63**(5), 1246–1255, ISSN 13652478 (doi: 10.1111/1365-2478.12224)

Lewis G, Osterberg E, Hawley R, Marshall HP, Meehan T, Graeter K, McCarthy F, Overly T, Thundercloud Z and Ferris D (2019) Recent precipitation decrease across the western Greenland ice sheet percolation zone. *Cryosph.*, **13**(11), 2797–2815, ISSN 1994-0424 (doi: 10.5194/tc-13-2797-2019)

Loewe F (1970) Screen Temperatures and 10m Temperatures. *J. Glaciol.*, **9**(56), 263–268, ISSN 0022-1430 (doi: 10.3189/S0022143000023571)

Margrave GF and Lamoureux MP (2019) *Numerical Methods of Exploration Seismology*. Cambridge University Press, ISBN 9781316756041 (doi: 10.1017/9781316756041)

Nelder JA and Mead R (1965) A Simplex Method for Function Minimization. *The Computer Journal*, **7**(4), 308–313, ISSN 0010-4620 (doi: 10.1093/comjnl/7.4.308)

Ng F and King EC (2011) Kinematic waves in polar firn stratigraphy. *J. Glaciol.*, **57**(206), 1119–1134, ISSN 0022-1430 (doi: 10.3189/002214311798843340)

294 Rupper S, Christensen WF, Bickmore BR, Burgener L, Koenig LS, Koutnik MR, Miège C and Forster
295 RR (2015) The effects of dating uncertainties on net accumulation estimates from firn cores. *J. Glaciol.*,
296 **61**(225), 163–172, ISSN 00221430 (doi: 10.3189/2015JoG14J042)
297 Spikes VB, Hamilton GS, Arcone SA, Kaspari S and Mayewski PA (2004) Variability in accumulation
298 rates from GPR profiling on the West Antarctic plateau. *Ann. Glaciol.*, **39**, 238–244, ISSN 02603055
299 (doi: 10.3189/172756404781814393)
300 Treitel S (1974) THE COMPLEX WIENER FILTER. *GEOPHYSICS*, **39**(2), 169–173, ISSN 0016-8033
301 (doi: 10.1190/1.1440419)
302 Ulaby FT, Fung AK and Moore RK (1986) *Microwave remote sensing: active and passive*, volume 3 of
303 *From Theory to Applications*. Artech House
304 Wharton RP, Hazen GA, Rau RN and Best DL (1980) Advancements In Electromagnetic Propagation
305 Logging. In *SPE Rocky Mt. Reg. Meet.*, Society of Petroleum Engineers, Society of Petroleum Engineers
306 (doi: 10.2118/9041-MS)
307 Wheeler HE (1958) Time-Stratigraphy. *Am. Assoc. Pet. Geol. Bull.*, **42**(5), 1047–1063, ISSN 0149-1423
308 (doi: 10.1306/0BDA5AF2-16BD-11D7-8645000102C1865D)
309 Yilmaz Ö (2001) *Seismic Data Analysis*. Society of Exploration Geophysicists, ISBN 978-1-56080-094-1
310 (doi: 10.1190/1.9781560801580)